Proc. U.S.-Japan Workshop on Smart Structures for Improved Seismic Performance in Urban Regions,
14 August 2001, Seattle WA, ed. K. Kawashima, B.F. Spencer, and Y. Suzuki, pp 225–236.

OPTIMAL DESIGN OF MR DAMPERS

Henri GAVIN, Jesse HOAGG and Mark DOBOSSY
Department of Civil and Environmental Engineering, Duke University
Durham, NC, USA, hpgavin@duke.edu

Abstract

The electro-magnetic components of an MR damper are characterized by multiple design variables which have a direct effect on the electrical power consumption of an MR device. Nonlinear magnetic behavior of the steel alloy and MR fluid is coupled to the non-Newtonian fluid mechanics of the MR suspensions in a method that minimizes the electrical power consumption and the inductive time constant while meeting a variety of conditions regarding the device's force capacity, size, and electrical characteristics. The paper closes with a comparison between ER and MR devices in the context of electrical power requirements.

Key Words: Magnetorheological damper, Electrorheological damper, Optimal Design, Nonlinear magnetization

INTRODUCTION

The MR device designed in this research is a commercial hydraulic cylinder through which an electro-magnetic piston pumps MR fluid. When a magnetic field passes through MR fluid, it develops a yield stress which must be achieved before the material will flow. The piston is wrapped in magnet wire and generates magnetic flux in the piston, cylinder, and MR fluid. When subjected to intense magnetic fields (1 T), the yield stress of the MR material increases from less than 0.1 kPa to roughly 100 kPa. This change in material properties is sufficient to increase damping forces by a factor of 10 or more.

There are two main design goals for the MR devices discussed in this paper. First, the dampers must have low electrical power consumption. And second, the force in the device must respond quickly to changes in the electric command signal. These objectives must be achieved such that several constraints are satisfied with regard to the force levels, magnetic fluxes, overall size of the device, and overall geometry of the device.

The design and applications of MR devices has been an area of recent interest due to the controllable characteristics of MR material. Work has been done to improve some of the key characteristics of MR fluids, such as increasing its yield stress and thereby allowing for a wider variety of applications (Tang et al. 1999). Significant work has been done on modeling the dynamic characteristics of MR devices, through a variety of approaches (Lee and Wereley 1999, Kordonsky 1993, Spencer et al. 1997, and Wereley et al. 1999). New approaches to developing MR devices are being explored and new designs are being tested (Kelso and Gordaninejad 1999, Stanway et al. 2000, Spencer et al. 1997, Lindler et al. 2000, Milecki 2001, and Gordaninejad and Kelso 2000). In addition, some work has been done on MR device design methods (Boelter and Janocha 1997) and device optimization (Jin et al. 1998). There are several important patents on MR devices (Carlson et al. 1994, Gordaninejad and Breese 1998, and Wolfe 1990).

DESIGN CONCEPT

Figure 1 illustrates the conceptual design of the MR damper. The spools of magnet wire, shown with the vertical hash marks, generate magnetic flux within the steel piston. Adjacent spools are wound in opposing directions and the magnetic flux forms three magnetic circuits. The flux in the magnetic circuit flows axially through the steel core of diameter D_c, beneath the windings, radially through the piston poles of length L_p, through a gap of thickness t_g, in which the MR fluid flows, and axially through the cylinder wall of thickness t_w. Figure 2 shows the flux intensity and directions as computed via a finite element analysis. Our MR damper design

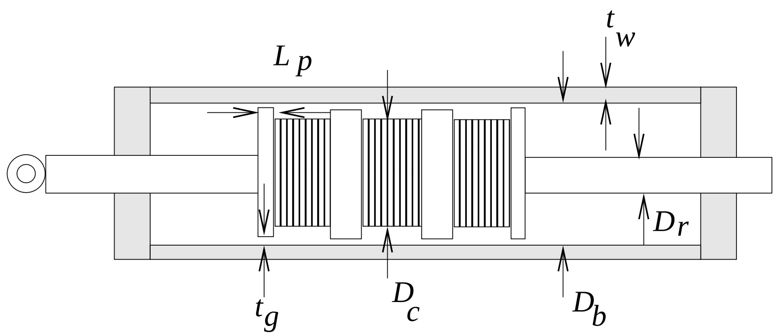

Figure 1: Diagram of the Conceptual MR Damper Design

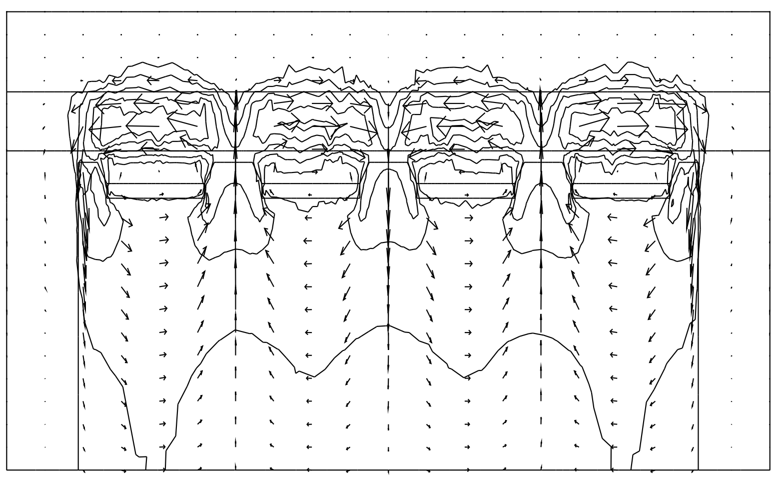

Figure 2: Finite Element Analysis of Conceptual MR Damper Design

involves six different physically dimensioned parameters. They are the diameter of the casing bore, D_b, the diameter of the piston rod, D_r, the thickness of the casing wall, t_w, the diameter of the core, D_c, the pole length, L_p, and the thickness of the gap, t_g.

NON-NEWTONIAN FLUID MECHANICS

The one-dimensional behavior of MR material undergoing simple shear is assumed to follow a Bingham constitutive model in which the applied shear stress is resisted by a flux-dependent yield stress, $\tau_y(B)$, and a flux-independent viscous stress, $\eta\dot{\gamma}$,

$$\tau(B_g, \dot{\gamma}) = \tau_y(B_g)\text{sgn}(\dot{\gamma}) + \eta\dot{\gamma} \tag{1}$$

where B_g is the magnetic flux density in the flow gap, η is the plastic viscosity, and $\dot{\gamma}$ is the shear rate. In this study we assume that the yield stress is proportional to the magnetic flux density, $\tau_y = \alpha B$, where $\alpha \approx 80$ kPa/T, and α is a material constant.

The pressure drop across the piston, Δp, also has yielding and viscous components (Gavin 1997).

$$\Delta p \approx 2.1\frac{\tau_y}{t_g} + \Delta p_N \tag{2}$$

where the Newtonian viscous component, Δp_N, is approximated by

$$\Delta p_N \approx \frac{12Q\eta(2N_s)L_p}{\pi(D_p + t_g)t_g^3} \tag{3}$$

where N_s is the number of spools of wire, Q is the volumetric flow rate, and D_p is the diameter of the piston. The constant 2.1 in Eq. (2) is empirical and reflects the particulate nature of MR fluids and their tendency to form lubricating films adjacent to the duct walls.

The force generated in the device, F, is the pressure drop times the piston cross sectional area and can be expressed as,

$$F = \Delta p\pi\frac{((D_p + t_g)^2 - D_r^2)}{4} \tag{4}$$

Assuming incompressibility, Q is related to the piston velocity, V_p, by

$$Q = V_p(\pi/4)(D_p^2 - D_r^2) \tag{5}$$

Thus, the device force may be obtained from the piston velocity, the device geometry, the MR fluid properties, and the magnetic flux density in the gap.

NON-LINEAR MAGNETO-STATICS

The small volume of MR fluid between the cylinder wall and the piston's magnetic poles is one link in a magnetic circuit which also includes the piston and the cylinder walls, as shown in Figure 2. This magnetic circuit can be analyzed using a magnetic Kirchoff Law,

$$\sum H_k l_k = Ni \tag{6}$$

where H_k is the magnetic field on induction in the kth link of the circuit and l_k is the effective length of that link. The number of turns of magnet wire is N and i is the current in the wire. The magnetic induction has units of Amp×turns/meter. At low magnetic fields, the flux density, B, increases in proportion to the induction, $B = \mu\mu_0 H$, where μ_0 is the magnetic permeability of free space ($4\pi \times 10^{-7}$ T·m/A) and μ is the relative permeability, which is a material constant. As the magnetic field becomes large, its ability to polarize the magnetic material diminishes. At a threshold field, H_c, the material is almost magnetically saturated and the saturation magnetization is,

$$J_b = B(H_c) - \mu_0 H_c \tag{7}$$

In our analysis, the following relationship is used to describe the magnetization curves,

$$H(B) = \frac{H_c B}{J_b} + \frac{1}{2s} \times (\frac{1}{\mu_0} - \frac{H_c}{J_b})(e^{\text{arcsinh}(s(B-J_b))} - e^{\text{arcsinh}(-sJ_b)}) \tag{8}$$

where s is the "sharpness" of the $B - H$ relationship. The magnetic flux density for the core, B_c, and the wall, B_w, are found from the conservation of magnetic flux, Φ_B.

$$\Phi_B = B_g A_g \tag{9}$$

$$B_c = \frac{\Phi_B}{A_c} \tag{10}$$

$$B_w = \frac{\Phi_B}{A_w} \tag{11}$$

where A_g, A_c, and A_w are the cross sectional areas of the gap, the core, and the cylinder wall respectively. We compute the flux density for each component in order to ensure that no part of the system becomes magnetically saturated.

By specifying B_g, the magnetic flux and flux densities in each component are calculated from Eq. (9), (10), and (11). Given magnetization parameters (H_c, J_b, and s) for the steel and the MR fluid in the device, the magnetic induction in each link of the magnetic circuit is computed with Eq. (8). Given B_g and H for each magnetic circuit component, the current required can be obtained from the magnetic circuit equation,

$$i = \frac{1}{N}(2H_g t_g + H_c(l_c + l_p) + H_p(D_p + t_w) + H_w(l_c + l_p)) \tag{12}$$

where N is the number of turns in one spool, l_c is the length of the core, l_p is the length of the poles. The magnetic induction in the gap, the pole, and the core are H_g, H_p, and H_c. The inductance, L, resistance, R, voltage, V, and the inductive time constant, T, are determined from,

$$L = \frac{N_s N \Phi_B}{i} \tag{13}$$

$$R = rN\pi D_c N_s \tag{14}$$

$$V = iR \tag{15}$$

$$T = \frac{L}{R} \tag{16}$$

where r is the resistance per unit length of the magnet wire. Variables defining the coil are the number of spools, N_s, the number layers of windings in each spool, N_l, and the wire gage.

CONSTRAINED OPTIMIZATION PROBLEM

Our objective in designing the damper is to minimize the time constant of the device and the electric power consumption of the device,

$$J = \frac{L}{R} + \beta iR \tag{17}$$

where β is a weighting coefficient.

A commercial hydraulic cylinder was modified for this device and several geometric properties such as the diameter of the cylinder and the wall thickness were fixed. The diameter of the outer wall, D_w, is 46.228 mm, the thickness of the wall, t_w, is 3.556 mm, and the diameter of the piston rod, D_r, is 15.875 mm.

Most of the design parameters directly influence the behavior of the magnetic circuit, and by choosing the parameters intelligently, MR devices with fast response times and low power requirements can be designed.

At high magnetic fields, magnetic materials become magnetically saturated. To balance the power requirements of the device and the flux density in the MR material, it is advantageous to design the magnetic circuit in such a way that under operating conditions all of the components are below their saturation fields. An additional benefit of operating at lower flux densities is that remnant magnetization of the magnetic circuit and MR material is diminished. Therefore, the flux density in the steel was bounded by a maximum of 1.5 T. The current cannot exceed the current rating of the wire.

The device is optimized by adjusting the design parameters t_g, L_p, N_s, N_l, N, B_g, D_c, and the wire gauge such that the following conditions are satisfied: $B_c < 1.5$ T, $B_w < 1.5$ T, $F_L < 5.0$ kN, $F_H > 4.1$ kN, $\frac{F_H}{F_L} > 10$, $T < 0.10$ s, $D_c < D_p - 2T_c$, $(L_c + 2L_p) \times N_s < 0.25$ m, $i < I_{max}$, and $V < 24$ V. In these inequality constraints, T_c is the thickness of the coil windings, I_{max} is the current rating of the wire, F_H is the device force at a piston velocity of 2 cm/s and maximum current in the coil, and F_L is the device force at a piston velocity of 30 cm/s and zero current in the coil. This constrained optimization problem was solved using a sequential least squares method.

DESIGN SENSITIVITY ANALYSIS

A sensitivity analysis using the Hessian of the objective function with respect to the design parameters was performed on the optimal design to determine manufacturing tolerances. The relative parameter variations giving rise to a 10 percent increase in the objective function are ±30% for t_g, ±7% for B_g, ±9% for D_c, ±10% for L_p, and ±28% for N.

Many parameters are discrete variables. The wire gage, the number of layers, and the number of spools have a small finite number of possibilities. The wire gage was limited to 7 values from 16 gage to 28 gage. The number of layers is limited by the maximum piston diameter and the gage of wire. The number of spools is limited by the maximum piston length. However, to achieve the desired force level, many combinations of wire gage, layers, and spools may be used. Optimal designs were calculated for every combination of these discrete parameters. For each optimal design, the electric power requirement was calculated. The electric power requirements for designs using three, four, and five spools are shown in Figures 3, 4, and 5 respectively. The optimal design was found to have 20 gage wire, with 4 spools and 4 layers and an electrical power requirement of 60 W. There were no feasible designs with wire sizes smaller then 22 gage, and very few feasible designs with more than 4 layers or less then 2 layers. Figure 6 shows the final design of the MR Device.

TESTING AND MODELING

The assembled MR device was tested with harmonic and random dynamic displacements applied by a servo-hydraulic testing system. In sine-sweep tests, frequencies ranged from 0.5 to 10 Hz. The device displacement, device force, and coil voltage were recorded digitally. From this data, the device velocity was calculated with central differences.

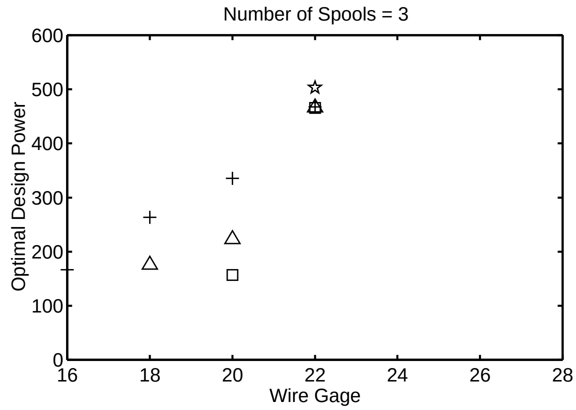

Figure 3: Power vs. Wire Gage for 2 Layers (plus), 3 Layers (triangle), 4 Layers (square), and 5 Layers(star) with Three Spools

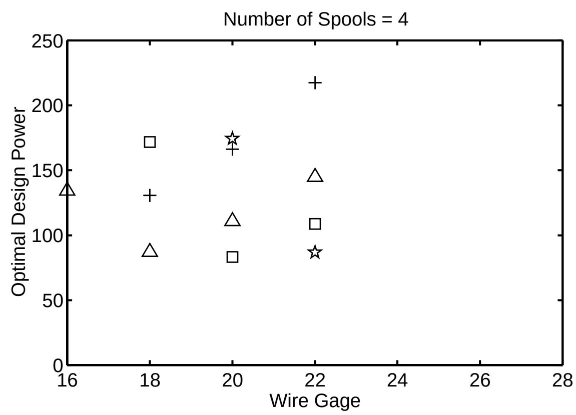

Figure 4: Power vs. Wire Gage for 2 Layers (plus), 3 Layers (triangle), 4 Layers (square), and 5 Layers(star) with Four Spools

Figure 5: Power vs. Wire Gage for 2 Layers (plus), 3 Layers (triangle), 4 Layers (square), and 5 Layers(star) with Five Spools

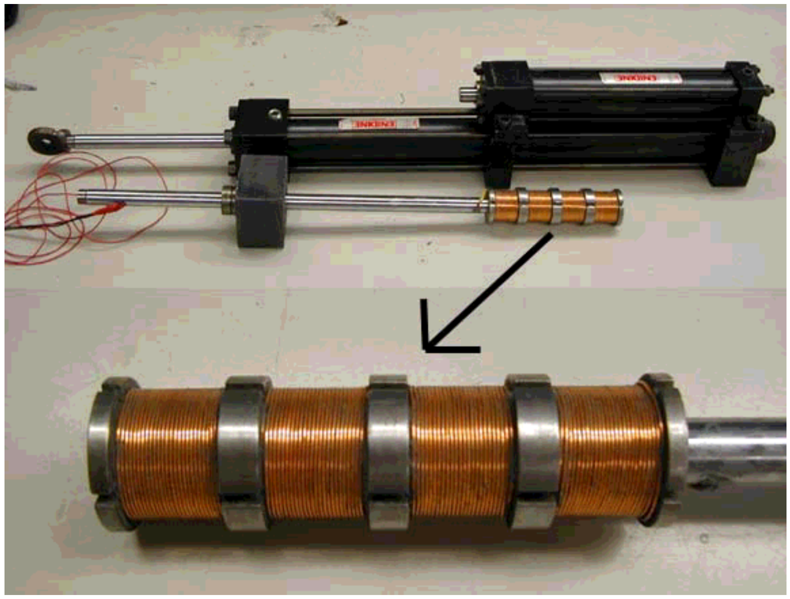

Figure 6: Final Design of the MR Device

The response of the device to switching electrical currents is shown in Figure 7. The data shows a maximum force of 4 kN, generated at 10 amps of current through the device. When the device is turned off, forces of around 0.30 kN are generated. When turned on, the device can develop an increase in force by a factor of ten, in under 50 milliseconds. When turned off, the device returns to low forces in less then 20 milliseconds. These are within the constraints of the intended design.

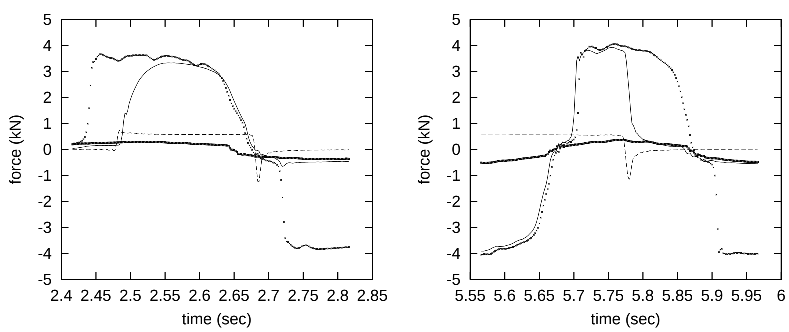

Figure 7: Device response for switching on (left) and for switching off (right)

An algebraic model utilizing the hyperbolic tangent function was applied to the data.

$$f(x, \dot{x}, V) = f_0(V) \tanh\left(\frac{x}{d_0} + \frac{\dot{x}}{v_0}\right) + k_0 x + c_0 \dot{x}. \tag{18}$$

In this expression, the yield force level, $f_0(V)$, is controllable, whereas the post-yield stiffness, k_0, and the plastic viscosity, c_0, are assumed to be insensitive to changes in the magnetic field. The details of the behavior in the pre-yield region are captured by the parameters d_0 and v_0 in the argument of the hyperbolic tangent. As this model has no dynamic states, it does not capture the frequency dependent visco-elastic behavior of the device. Nonetheless, it provides a closed form solution for the device force. Furthermore, an inverse model for the device behavior, which is useful for feedback linearization, is easily derived. Assuming that the yield force follows a power-law relationship with the voltage $f_0(V) = \alpha V^n$, and given the velocity and displacement across the device, the voltage V required to produce the desired damper force f is

$$V(x, \dot{x}, f) = \left[\frac{f - k_0 x - c_0 \dot{x}}{\alpha \tanh(x/d_0 + \dot{x}/v_0)}\right]^{\frac{1}{n}}. \tag{19}$$

It is also possible to develop the following dynamic state equation for an MR damper.

$$\begin{aligned} \frac{d}{dt}\begin{bmatrix} x_0 \\ \dot{x}_0 \end{bmatrix} &= \begin{bmatrix} 0 & 1 \\ -(k_0+k_1)/m_0 & -(c_0+c_1)/m_0 \end{bmatrix}\begin{bmatrix} x_0 \\ \dot{x}_0 \end{bmatrix} \\ &+ \begin{bmatrix} 0 & 0 \\ k_1/m_0 & c_1/m_0 \end{bmatrix}\begin{bmatrix} x \\ \dot{x} \end{bmatrix} \\ &+ \begin{bmatrix} 0 \\ -1/m_0 \end{bmatrix} f_0 \tanh(\dot{x}_0/V_r). \end{aligned} \tag{20}$$

$$\hat{f} = \begin{bmatrix} -k_1 & -c_1 \end{bmatrix}\begin{bmatrix} x_0 \\ \dot{x}_0 \end{bmatrix} + \begin{bmatrix} k_1 & c_1 \end{bmatrix}\begin{bmatrix} x \\ \dot{x} \end{bmatrix} \tag{21}$$

Figures 8 and 9 show the force versus displacement, force versus velocity, and force versus time plots for the MR damper at low and high frequency excitation respectively. The plots show the experimental data, the algebraic models, and the dynamic models for the damper at both 0 amps and 10 amps. Using optimization curve-fitting routines, the algebraic model and

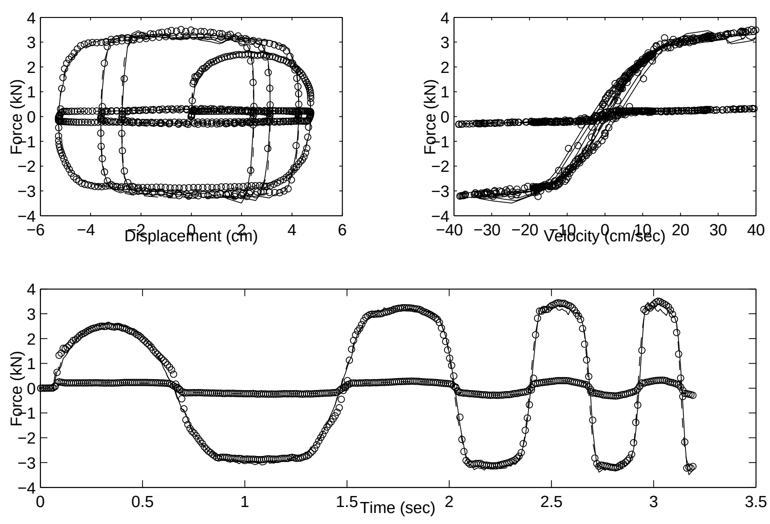

Figure 8: Damper Data (circles), Algebraic Model (dashed line), and Dynamic Model (solid line) at 0 Amps and 10 Amps for Low Frequency Excitation

the dynamic model were fit to data for the device working at 0 Amps, 2 Amps, 4 Amps, 6 Amps, 8 Amps, and 10 Amps. The algebraic model for the device at 0 Amps was fit using the following coefficient values, $k_0 = 0.00326 \pm 0.000180$ kN/cm, $c_0 = 0.00339 \pm 2.91 \times 10^{-5}$ kN/cm/s, $f_0 = 0.166 \pm 0.000571$ kN, $d_0 = 154$ cm/s, and $v_0 = 0.688 \pm 0.0644$ cm/s. And for the device at 10 Amps, $k_0 = 0.000116 \pm 0.00150$ kN/cm, $c_0 = 0.00811 \pm 0.000204$ kN/cm/s, $f_0 = 2.99 \pm 0.00480$ kN, $d_0 = 110 \pm 13.0$ cm/s, and $v_0 = 10.688 \pm 0.0550$ cm/s. The dynamic model for the device at 0

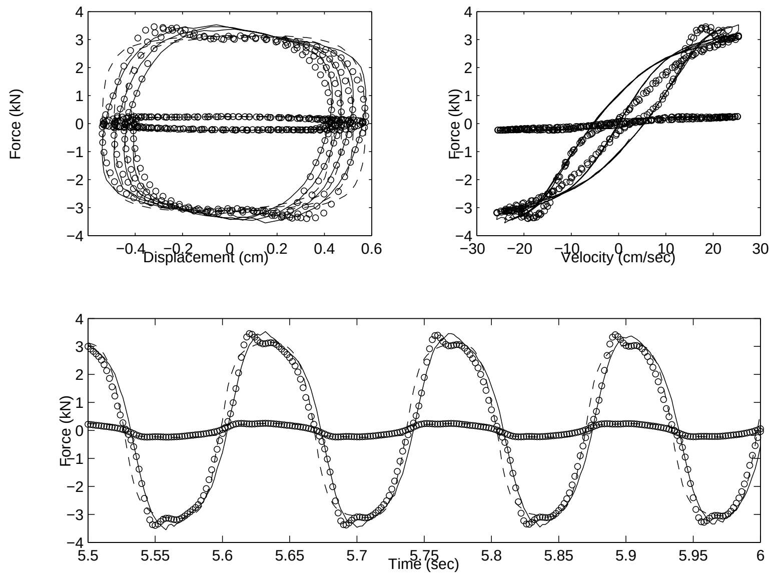

Figure 9: Damper Data (circles), Algebraic Model (dashed line), and Dynamic Model (solid line) at 0 Amps and 10 Amps for High Frequency Excitation

Amps was fit using $k_0 = 0.00009$ kN/cm, $c_0 = 0.00682$ kN/cm/s, $f_0 = 0.203$ kN, $m_0 = 0.000450$ kN/cm/s^2, $k_1 = 2.59$ kN/cm, $c_1 = 0.203$ kN/cm/s, and $V_r = 3.11$ cm/s. The dynamic model for the device operating at 10 Amps is $k_0 = 0.00075$ kN/cm, $c_0 = 0.0641$ kN/cm/s, $f_0 = 3.66$ kN, $m_0 = 0.000787$ kN/cm/s^2, $k_1 = 38.9$ kN/cm, $c_1 = 0.146$ kN/cm/s, and $V_r = 12.54$ cm/s.

ELECTRICAL POWER CONSIDERATIONS FOR ER AND MR DEVICES

ER devices are electrically capacitive and require high voltages; MR devices are electrically inductive and require moderate currents. To rapidly apply power (charge) to an ER device, it is advantageous to temporarily send more current than the leakage current to the devices. (The leakage current is the voltage (i.e. 5 kV) times $\rho Ch/\eta$, where ρ is the current density, C is the capacitance, h is the distance between the electrodes, and η is the plastic viscosity.) To rapidly apply power (i.e., current) to an MR device, one should over-drive the device's voltage. Removing power (charge) from ER devices is a simple matter of shorting the high-voltage electrodes of the device to ground, through a power resistor. (RC is small because C is small.) To safely dissipate the current in an MR device, a resistor in parallel with a Zener is placed in parallel with the coil. When the MR switch is closed only a small current passes through the parallel resistors. However, when the switch opens, the current through the resistors changes direction, and all the current in the coil passes through the resistor and dissipates rapidly. (L/R is small because R is large.)

The analysis of the power requirements for an ER device is more straight forward than for an MR device. The design of the magnetic circuit entails multiple variables, as outlined above, which allows the designer to optimize various electro-magnetic attributes of the MR device, such as power.

The net surface area of the electrodes in an ER device that achieves a dynamic range of P at mechanical power P_m, with a material yield stress τ_y and viscosity η and a gap size h is approximately

$$A = 2.7(P-1)\frac{\eta P}{\tau_y^2 h} \tag{22}$$

The capacitance of the device is $C = \epsilon A/h$, and the steady state current is ρA, where ϵ is the permittivity of the ER material and ρ is the current density. If the device is switched on and off with a period T, then the average electrical power requirement P_e is

$$P_e = \frac{CV^2}{4T} + \frac{V i_{DC}}{2}\left[1 - \frac{CV}{(i_p - i_{DC})T}\right], \tag{23}$$

where V is the power supply voltage, i_p is the peak current output by the power supply, and i_{DC} is the steady-state current drawn by the device. Using these expressions and properties for a particular ER material it is possible to relate the electrical power, P_e, required to regulate an amount of mechanical power, P_m at a switching rate T. As an example, the device/material combination described in table 1 result in ER and MR devices with the efficiencies shown in figure 11. The ER and MR materials used in this example are commercially available. Note that in ER devices increasing power supply current and increasing gap reduces the charging response times. Any water absorption of the ER material will result in a significant rise in the current density. Should the current density reach about 1 Amp/m^2, the electro-mechanical efficiency of the device would be seriously compromised.

Table 1: Electro-mechanical efficiency for ER and MR devices

Material	**TX-ER8 at 4 kV/mm**	**MRF-240BS at 1 Tesla**
Current Draw	0.13 Amp/sq.m	150 kA·turns/m
Viscosity (at 0 kV), η	0.035 Pa·sec	0.5 Pa·sec
Yield Stress, τ_{y}	5 kPa	80 kPa
Dynamic Range, $F_{\mathrm{on}}/F_{\mathrm{off}}$	10 (at 50 cm/sec)	10 (at 50 cm/sec)
Flow Gap, h	1.6 mm	0.8 — 2.8 mm
Electrical	$C = 0.001$ — 0.050 μF	$L = 0.015$ — 0.5 Henry
Field limited by:	dielectric break-down	magnetic saturation
Response Time	0.1 — 10 ms	0.1 — 12 ms
Power Supply Current, $i_{\max}$	0.3 Amp (peak) 0.001 — 0.250 Amp (continuous)	4.9 Amp
Power Supply Voltage, $V_{\max}$	6400 Volt	200 Volt (peak) 4 — 24 Volt (continuous)

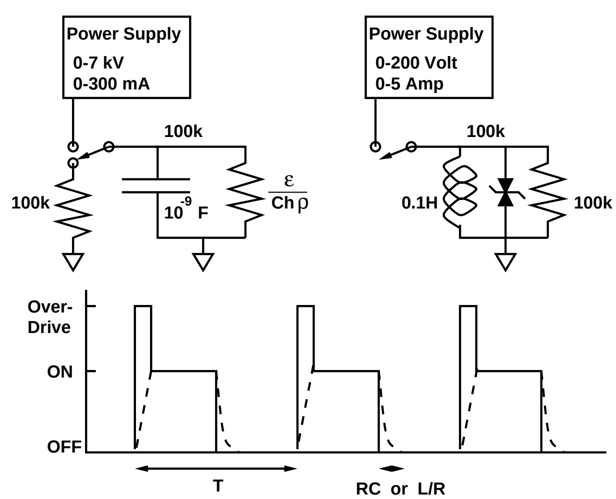

Figure 10: Electrical circuits for rapid operation of ER and MR devices.

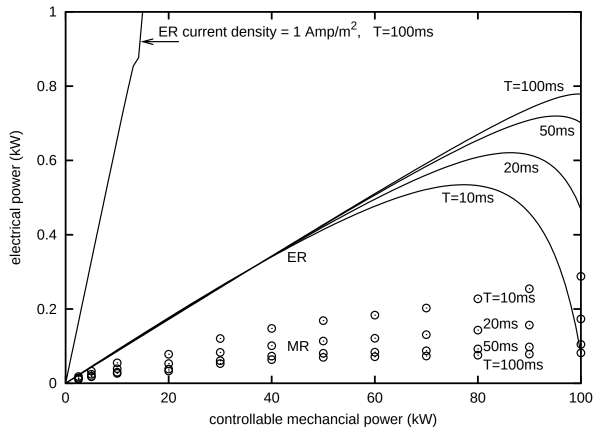

Figure 11: Electrical power requirements for switching ER and MR devices.

ACKNOWLEDGMENTS

This material is based on work supported by the National Science Foundation under Award No.s CMS-9624949 and CMS-9900193, and by Enidyne Corporation. The authors are grateful to Professor Pradeep Phule for providing samples of MR materials and to Nippon Shokubai Corporation for providing samples of ER materials for this research. Any opinions, findings, and conclusions or recommendations expressed in this publication are those of the authors and do not necessarily reflect the views of the sponsors.

REFERENCES

1. Boelter, R. and Janocha, H. (1997). "Design rules for MR fluid actuators in different working modes." *Proc. SPIE*, Vol. 3045, 148-159.

2. Carlson, J.D. and M.J. Chrzan (1992) "Magnetorheological Fluid Dampers," US Patent 5,277,281.

3. Dyke, S.J., Spencer, B.F., Sain, M.K., et al. (1998). "An experimental study of MR dampers for seismic protection." *Smart Materials and Structures*, Vol. 7, No. 5, 693-703.

4. Gavin, H.P. (1997). "The Effect of Particle Concentration Inhomogeneities on the Steady Flow of Electro- and Magneto-Rheological Materials." *Journal of Non-Newtonian Fluid Mechanics*, Vol. 71, 165-182.

5. Gavin, H.P. (1998). "Design method for high-force electrorheological dampers." *Smart Materials and Structures*, Vol. 7, No. 5, 664-673.

6. Gavin, H.P., Hanson, R.D., and Filisko, F.E. (1996). "Electrorheological dampers, Analysis and design." *Journal of Applied Mechanics*, Vol. 63, No. 3, 669-675.

7. Gordaninejad, F. (1998) "Magnetorheological Fluid Damper," International Patent 98/04846.

8. Gordaninejad, F. and Kelso, S.P. (2000). "Fail-safe magneto-rheological fluid dampers for off-highway, high-payload vehicles." *Journal of Intelligent Material Systems and Structures*, Vol. 11, No. 5, 395-406.

9. Jin, D., Chen, J., and Huang, J. (1998). "Analysis and design of device using electrorheological/magnetorheological fluid with variable stiffness." *Proc. SPIE*, Vol 3201, 204-212.

10. Kelso, S.P. and Gordaninejad, F. (1999). "Magnetorheological fluid shock absorbers for off-highway high-payload vehicles." *Proc. SPIE*, Vol. 3672, 44-54.

11. Kordonsky, W.I. (1993). "Magnetorheological effect as a base of new devices and technologies." *Journal of Magnetism and Magnetic Materials*, Vol. 122, No. 1-3, 395-398.

12. Lee, D.Y. and Wereley, N.M. (1999). "Quasi-steady Herschel-Bulkley analysis of electro- and magneto-rheological flow mode dampers." *Journal of Intelligent Material Systems and Structures*, Vol. 10, No. 10, 761-769.

13. Li, W.H., Yao, G.Z., Chen, G., Yeo, S.H., and Yap, F.F. (2000). "Testing and steady state modeling of a linear MR damper under sinusoidal loading." *Smart Materials and Structures*, Vol. 9, No. 1, 95-102.

14. Lindler, J.E., Dimock, G.A., and Wereley, N.M. (2000). "Design of a megnetorheological automotive shock absorber." *Proc. SPIE*, Vol. 3985, 426-437.

15. Milecki, A. (2001). "Investigation and control of magneto-rheological fluid dampers." *International Journal of Machine Tools & Manufacture*, Vol. 21, No. 3, 379-391.

16. Patten, W.N., Mo, C., Kuehn, J., and Lee, J. (1998). "A primer on design of semiactive vibration absorbers (SAVA)." *Journal of Engineering Mechanics*, Vol. 124, No. 1, 61-68.

17. Stanway, R., Sims, N.D., and Johnson, A.R. (2000). "Modeling and control of a magneto-rheological vibration isolator." *Proc. SPIE*, Vol. 3989, 184-193.

18. Sims, N.D., Peel, D.J., Stanway, R., Johnson, A.R., and Bullough, W.A. (2000). "The electrorheological long-stroke damper: A new modeling technique with experimental validation." *Journal of Sound and Vibration*, Vol. 229, No. 2, 207-227.

19. Spencer, B.F., Dyke, S.J., Sain, M.K., and Carlson, J.D. (1997). "Phenomenological model for magnetorheological dampers." *Journal of Engineering Mechanics*, Vol. 123, No. 3, ASCE, 230-238.

20. Tang, X., Zhang, X., and Tao, R. (1999). "Flexible fixture device with magneto-rheological fluids." *Journal of Intelligent Material Systems and Structures*, Vol. 10, No. 9, 690-694.

21. Wereley, N.M., Kamath, G.M., and Madhavan, V. (1999). "Hysteresis modeling of semi-active magnetorheological helicopter dampers." *Journal of Intelligent Material Systems and Structures*, Vol. 10, No. 8, 624-633.

22. Wereley, N.M. and Pang, L. (1998). "Nondimensional analysis of semi-active electrorheological and magnetorheological dampers using approximate parallel plate models." *Smart Materials and Structures*, Vol. 7, No. 5, 732-743.

23. Wereley, N.M., Pang, L., and Kamath, G.M. (1998). "Idealized hysteresis modeling of electrorheological and magnetorheological dampers." *J. Intelligent Material Systems and Structures*, Vol. 9, No. 8, 642-649.

24. Wolfe, P.T. (1990) "Hybrid Analog Digital Control Method and Apparatus for Estimation of Absolute Velocities in Active Suspension Systems," US Patent 4,953,089.